# MODELLING FRICTION AND HEAT TRANSFER IN TURBULENT FORCED CONVECTION OVER POROUS SUBSTRATES

**Aneek Chakraborty**
Department of Aerospace Engineering
Delft University of Technology
Kluyverweg 2, 2629 HS, Delft
The Netherlands
a.chakraborty@tudelft.nl

**Stefan Hickel**
Department of Aerospace Engineering
Delft University of Technology
Kluyverweg 2, 2629 HS, Delft
The Netherlands
s.hickel@tudelft.nl

**Davide Modesti**
Gran Sasso Science Institute
viale Francesco Crispi 7, L'Aquila,
Italy
davide.modesti@gssi.it

## Abstract

Direct numerical simulations are conducted to investigate turbulent forced convection over porous cubic lattices with porosities ranging from 50% to 87% at friction Reynolds numbers up to 1500 and Prandtl numbers 0.5, 1, and 2. As porosity increases, a clear transition is observed from streaky near-wall turbulence to spanwise-coherent structures, enhancing turbulent mixing and heat transfer. The mean velocity and temperature profiles indicate that both drag and heat transfer increase with porosity and Reynolds number, quantified in terms of velocity and temperature deficits. We find that the velocity and temperature deficits can be modeled as functions of the inverse of the streamwise Forchheimer permeability, which appears to be the appropriate reference length scale for turbulent grazing flows over porous surfaces.

## Introduction

Turbulent forced convection in internal flows plays a crucial role in many industrial applications across mechanical and aerospace engineering. Common devices relying on forced convection include heat exchangers, fuel cells, turbine blades, and rocket nozzles. One of the most widely employed strategies to enhance convective heat transfer is the introduction of surface roughness; however, this typically comes at the cost of increased pressure drag (Ligrani, 2013; Chung *et al.*, 2021). In this context, porous surfaces present a promising alternative. Although flow across porous surfaces generally incurs a higher pressure drop, the corresponding increase in heat transfer can be substantial.

For turbulent flows over rough or porous surfaces, accurately predicting momentum and scalar transport is considerably more challenging than for smooth-wall flows. Over the past decades, computational and analytical efforts have led to predictive models for heat transfer over roughness layers (Yaglom & Kader, 1974; Brutsaert, 1975; Kays & Crawford, 1980; Peeters & Sandham, 2019; Zhong *et al.*, 2023) . In contrast, predictive models for turbulent grazing flow over porous surfaces remain largely undeveloped, leaving heat transfer in forced convection over porous media an open and elusive problem.

Both surface roughness and permeability strongly influence the near-wall flow over porous surfaces, as demonstrated in numerical studies (Breugem & Boersma, 2005; Nishiyama *et al.*, 2020) and experimental investigations (Efstathiou & Luhar, 2020). Direct numerical simulations (DNS) of porous lattices and foams reveal a transition from streaky near-wall turbulence to spanwise-coherent structures with increasing friction Reynolds number $Re_\tau$ (Khorasani *et al.*, 2024; Kuwata & Suga, 2024). Comparable behavior is observed in acoustic liners, where wall-normal nonlinear permeability was shown to govern turbulent grazing flow (Shahzad *et al.*, 2023).

Studies on heat transfer in turbulent forced convection over porous surfaces further indicate that heat transfer increases with porosity (Chandesris *et al.*, 2013; Nishiyama *et al.*, 2020). While significant progress has been made in developing predictive models for drag and heat transfer over roughness layers, equivalent models for porous surfaces remain scarce. The present work aims to address this gap by developing predictive models for turbulent forced convection over porous lattices, based on an extensive DNS database.

## Methodology

We perform DNS of grazing turbulent channel flow over porous lattices. The computational domain has dimensions $3\delta \times 2(\delta + h) \times 1.5\delta$, except for cases $S1500$ and $H1500$, where a larger domain of size $6\delta \times 2(\delta+h) \times 3\delta$ is employed. The half-channel height is denoted by $\delta$, and $h$ represents the height of the porous substrate, as illustrated in Figure 1.

The porous substrate consists of a cubic lattice configuration, with ligaments of square cross-section having side length $0.0388\delta$. The pore sizes vary in the streamwise, wall-normal, and spanwise directions, ranging from $0.038\delta$ to $0.111\delta$. This variation enables a parametric study of volume porosity, with values of 50% (denoted by $L$), 71% ($M$), and 87% ($H$), as shown in Figure 1. Smooth-wall reference cases are denoted

| Cases | $Re_b$ | $Re_\tau$ | $\sqrt{K_x^+}$ | $\sqrt{K_y^+}$ | $\sqrt{K_z^+}$ | $1/\alpha_x^+$ | $1/\alpha_y^+$ | $1/\alpha_z^+$ | $\Delta U^+$ | $\Delta\Theta_2^+$ | $\Delta\Theta_1^+$ | $\Delta\Theta_{0.5}^+$ |
|---|---|---|---|---|---|---|---|---|---|---|---|---|
| S260 | 8800 | 262.08 | - | - | - | - | - | - | - | - | - | - |
| S500 | 18800 | 509.27 | - | - | - | - | - | - | - | - | - | - |
| S700 | 26000 | 676.34 | - | - | - | - | - | - | - | - | - | - |
| S1500 | 63000 | 1497.86 | - | - | - | - | - | - | - | - | - | - |
| L260 | 9100 | 275.82 | 1.04 | 1.12 | 1.04 | 1.11 | 0.79 | 1.11 | 1.05 | 0.30 | 0.11 | 0.25 |
| L500 | 18200 | 511.91 | 1.91 | 2.06 | 1.91 | 2.06 | 1.46 | 2.06 | 1.53 | 2.50 | 0.90 | 0.45 |
| L700 | 24960 | 687.64 | 2.59 | 2.79 | 2.59 | 2.77 | 1.97 | 2.77 | 1.98 | 3.40 | 1.20 | 0.65 |
| M260 | 7800 | 258.06 | 1.78 | 2.32 | 3.09 | 2.63 | 3.14 | 4.78 | 1.89 | 4.03 | 1.50 | 0.85 |
| M500 | 14820 | 500.69 | 3.44 | 4.51 | 6.01 | 5.11 | 6.09 | 9.28 | 3.72 | 8.60 | 4.00 | 1.85 |
| M700 | 21060 | 688.41 | 4.75 | 6.19 | 8.24 | 7.02 | 8.38 | 12.75 | 4.80 | 9.50 | 4.50 | 2.05 |
| H260 | 4940 | 245.65 | 5.31 | 4.53 | 5.31 | 14.13 | 8.43 | 14.13 | 6.91 | 13.40 | 7.45 | 3.85 |
| H500 | 10140 | 506.19 | 11.08 | 9.45 | 11.08 | 29.13 | 17.56 | 29.13 | 8.85 | 15.20 | 9.25 | 5.45 |
| H700 | 13988 | 699.97 | 15.13 | 12.90 | 15.13 | 40.28 | 24.02 | 40.28 | 9.69 | 15.36 | 9.65 | 5.90 |
| H1500 | 29380 | 1496.74 | 32.35 | 27.58 | 32.35 | 86.12 | 51.36 | 86.12 | 11.67 | 15.37 | 9.95 | 6.50 |

Table 1. **Description of cases:** Bulk Reynolds number $Re_b = 2(\delta+h)U_b/\nu$ is reported based on the entire channel height and $Re_\tau = 2\delta u_\tau/\nu$ on half free channel height. The '+' superscript represents the non-dimensionalization of the quantity by viscous wall units ($\delta_\nu = \nu/u_\tau$). The permeability Reynolds numbers in the streamwise, wall-normal and spanwise directions are given as $\sqrt{K_x^+}$, $\sqrt{K_y^+}$ and $\sqrt{K_z^+}$. The viscous scaled inverse of Forchheimer permeabilities are given as $1/\alpha_x^+$, $1/\alpha_y^+$, and $1/\alpha_z^+$.The momentum deficit is given as $\Delta U^+$, and the temperature deficit is given as $\Theta_i^+$, where $i$ denotes $Pr$.

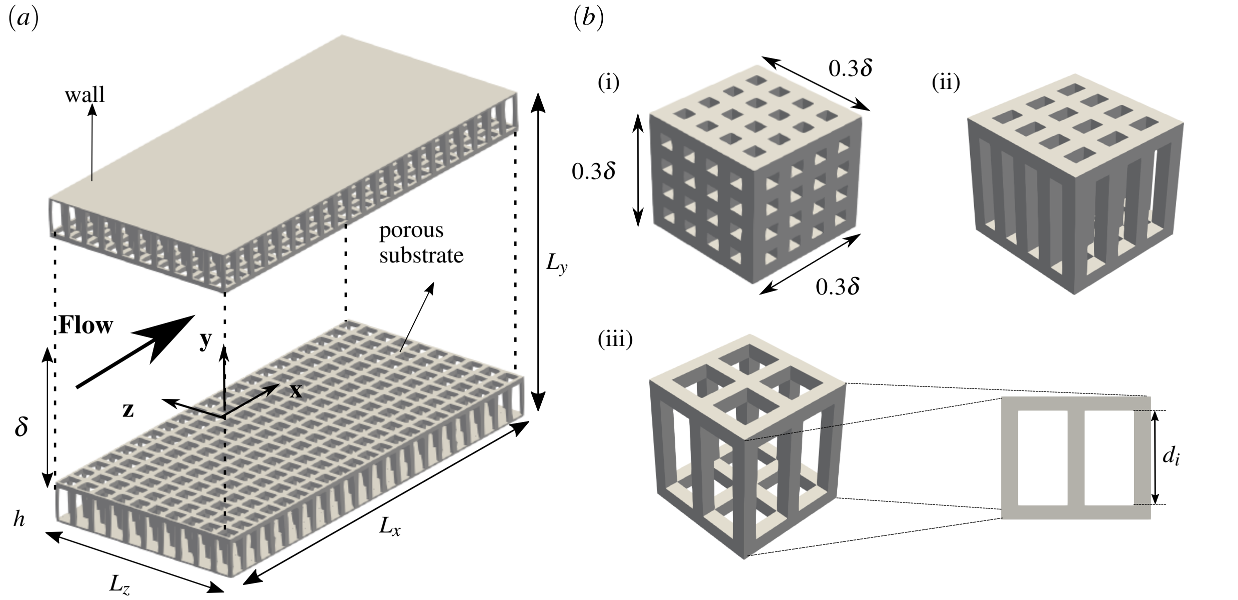


Figure 1. (a) Schematic of computational domain with $L_x$, $L_y$ and $L_z$ as the domain dimensions. ($L_x \times L_y \times L_z = 3\delta \times 2.6\delta \times 1.5\delta$); (b)Unit cells of porous geometries used for simulations for (i) $50\%(L)$, (ii) $71\%(M)$, and (iii) $87\%(H)$. The dimensions of the unit cell are also shown to be $0.3\delta \times 0.3\delta \times 0.3\delta$. Further, the pore size are also shown as $d_i$ where $i \in x,y,z$ for pores in three directions.

by $S$. A comprehensive summary of all simulations is provided in Table 1.

The porous unit cells are characterized using Stokes flow simulations conducted in OpenFOAM. The pressure drop is computed over a range of pore Reynolds numbers $Re_p$ from 0.1 to 1000. The Darcy–Forchheimer equation is employed:

$$\frac{\Delta P}{\Delta L}\frac{D^2}{\rho \nu U_t} = \frac{D^2}{K} + \sigma\alpha D Re_p, \tag{1}$$

where $\Delta P/\Delta L$ is the pressure gradient across the unit cell, $D$ is the pore hydraulic diameter, $\sigma$ is the ratio of the unit cell face

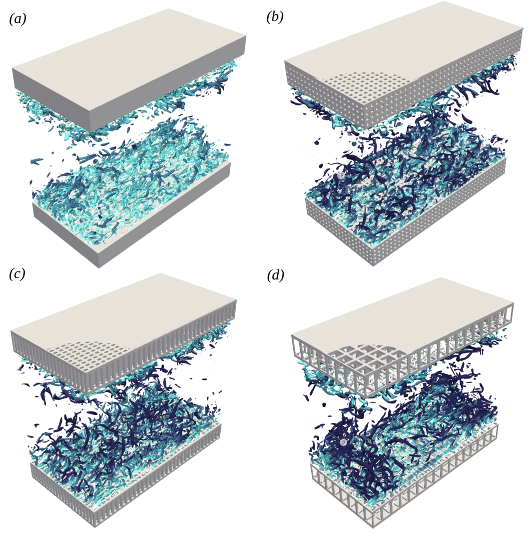


Figure 2. Isometric view of instantaneous flow field for *S*700 *(a)*, *L*700 *(b)*, *M*700 *(c)* and *H*700*(b)*. The flow field is visualized through Q-criterion coloured by streamwise velocity.

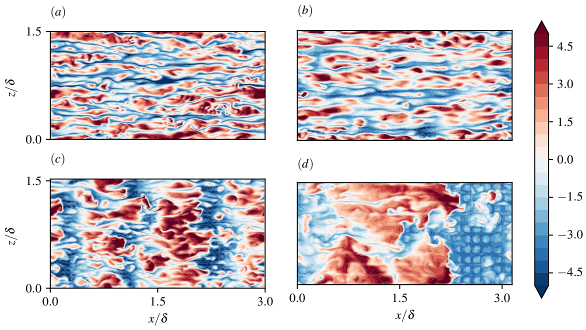


Figure 3. Instantaneous temperature fluctuations in wall units, are shown for $Pr = 1$ in a wall-parallel plane at $y^+ = 15$ for *S*700 (*a*), *L*700 (*b*), *M*700(*c*) and *H*700 (*d*).

area to the pore area, $U_t$ is the superficial inlet velocity, $\rho$ is the fluid density, and $\nu$ is the kinematic viscosity. The linear permeability $K$ and Forchheimer coefficient $\alpha$ are evaluated in each principal direction of the unit cell.

As reported in Table 1, increasing porosity leads to higher linear permeability and a decrease in the inverse of the Forchheimer term. This indicates that with increasing pore size, inertial effects become more significant, and the nonlinear contribution in the Darcy–Forchheimer relation becomes dominant.

A uniform grid is used with periodic boundary conditions in the streamwise and spanwise directions. In the wall-normal direction, grid stretching is applied to cluster points near the porous interface, while uniform spacing is maintained within the porous region to ensure at least 10 grid points per pore spacing. Isothermal no-slip boundary conditions are imposed on the fully resolved porous surfaces.

The incompressible Navier–Stokes equations and the passive scalar temperature equation are solved using a second-order staggered finite-difference solver (Pirozzoli *et al.*, 2016). The porous geometry is represented using an immersed boundary method (Deprati *et al.*, 2021). The friction Reynolds number $Re_\tau$ ranges from 260 to 1500, and for each case, the temperature field is solved for Prandtl numbers $Pr = 0.5, 1$, and 2.

The overbar denotes Reynolds averaging in time and over the periodic directions. Statistics are collected for at least $\Delta T u_\tau / h = 50$ to ensure convergence, and intrinsic averaging is applied, i.e., averages are computed only over the fluid region.

## Results

### Flow visualization

We start by visualizing the three-dimensional instantaneous flow field in figure 2, which presents the Q-criterion at $Re_\tau \approx 700$ for different porosities, alongside the smooth-wall reference case. For the smooth wall, the Q-criterion reveals vortical structures concentrated near the wall. These vortices are elongated in the streamwise direction and exhibit an inclination relative to the wall, primarily due to the influence of mean shear.

As the volume porosity increases, a clear change in vortex organization becomes apparent. Turbulent activity intensifies and extends farther away from the wall, indicating enhanced mixing not only near the wall but also within the channel core. With increasing permeability, the vortices gradually lose their characteristic alignment and become more isotropic, suggesting a substantial modification of the near-wall flow dynamics compared to the baseline smooth-wall case.

To further examine how thermal structures evolve with porosity, figure 3 shows contours of temperature fluctuations at $Pr = 1$ in a wall-parallel plane located at $y^+ + \ell_T^+ \approx 15$ (where $\ell_T$ denotes the virtual origin of turbulence). In the smooth-wall case (S700), distinct low- and high-speed streaks are clearly visible, representing the of the near-wall cycle. When wall permeability is introduced (case *L*700), similar streaky structures persist, although their streamwise extent is noticeably reduced. A comparable shortening of streak length with increasing permeability was reported by Breugem *et al.* (2006). This behaviour is associated with enhanced wall-normal velocity fluctuations, as also observed by Kuwata & Suga (2019) and Shahzad *et al.* (2022).

A more pronounced transition occurs at 71% porosity, where the streaky structures give way to shorter, more blob-like features, indicating a breakdown of the classical near-wall cycle. At even higher porosity (87%), the temperature fluctuations reveal the emergence of spanwise-coherent structures. Such structures have previously been reported over porous surfaces (Suga *et al.*, 2011; Manes *et al.*, 2011; Suga *et al.*, 2017) as well as over riblet surfaces (Garcia-Mayoral & Jimenez, 2011; Endrikat *et al.*, 2021).

### Virtual origin and mean profiles

The location of the wall for porous cases needs to be determined for comparison with smooth wall statistics. The impermeability condition is relaxed over a porous wall; therefore, the location of the wall perceived by the flow is not located at the interface between the free channel and the porous substrate but shifted inside the porous medium. This shifted location, where it can be the outer flow perceives the 'wall' is known as the virtual origin. In the present work, we use the approach adopted by Ibrahim *et al.* (2021), where we shift the Reynolds shear stress profile by a virtual origin shift $\ell_T$ to match the smooth wall case at matched Reynolds number as much as possible, see figure 5. A good match between the porous and smooth wall cases is observed, apart from the 87%

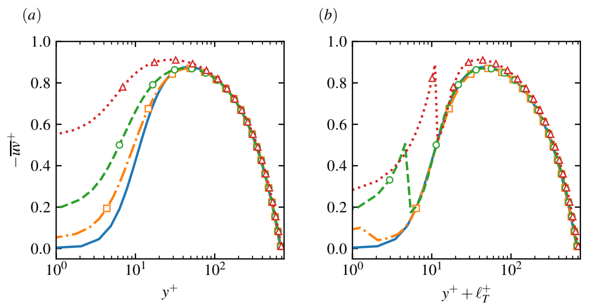


Figure 4. Reynolds shear stress $\overline{uv}+$ profiles plotted with wall-normal coordinate $y^+$ before *(a)* and after *(b)* virtual-origin shift. Blue solid lines shows $S700$ case, orange dash-dotted lines shows $L700$, green dashed line shows $M700$ and red dotted line refers to $H700$ case.

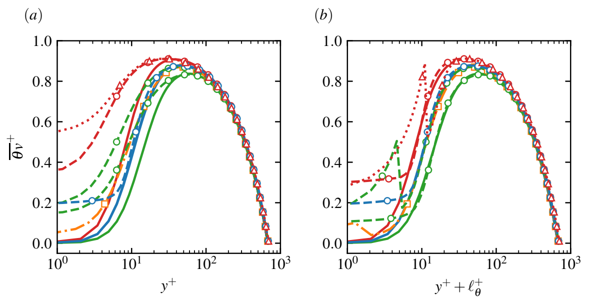


Figure 5. Wall-normal turbulent heat flux $\overline{\theta v}^+$ profiles plotted with wall-normal coordinate $y^+$ before *(a)* and after *(b)* $Pr$ premultiplied virtual-origin shift. Blue lines shows $Pr = 1$, green lines shows $Pr = 0.5$ and red line shows $Pr = 2$. Solid lines refer to $S700$ case and dashed lines refer to $M700$ case.

porosity cases, for which the Reynolds shear stress distribution is inherently slightly different from the reference.

At $Pr = 1$, the virtual origin shift of the temperature approximately coincides with that of momentum, however for $Pr \neq 1$, this might not be the case. Therefore there is need to incorporate $Pr$ into the virtual origin shift for temperature. Given the linear relationship of the temperature profile in the viscous sublayer with the wall distance $\theta = Pry^+$, we report temperature data in this form and calculate the thermal virtual origin by shifting the turbulent heat flux by $\ell_\theta$ to match the smooth wall data in the inner layer, as shown in figure 5 for flow case $M700$.

In figure 6 we present the mean streawmise velocity and the mean temperature for case M700, for different Prandtl numbers. The velocity and temperature profiles show a positive downward shift, compared to the smooth wall data, indicating higher drag and heat transfer, both of which increase with the volume porosity. This shift is quantified by $\Delta U^+ = U_s^+ - U_p^+$ and $\Delta\Theta^+ = \Theta_s^+ - \Theta_p^+$, where $s$ and $p$ denote smooth and porous wall, for velocity and temperature respectively.

## Mean velocity deficit

Modelling the velocity and temperature profile for turbulent flow through porous channels requires the modelling of the smooth counterpart and the deficit function. Models for the smooth wall velocity (Nagib & Chauhan, 2008) and temperature profile (Pirozzoli & Modesti, 2024), are readily available in literature but the challenge remains in finding suitable approximations for the momentum and temperature shifts $\Delta U^+(\ell^+)$ and $\Delta\Theta^+(\ell^+, Pr)$.

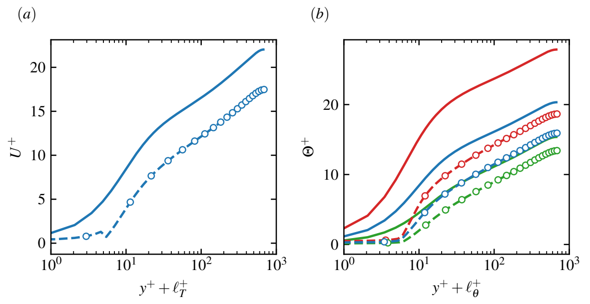


Figure 6. *(a)* Mean streamwise velocity plotted with wall-normal distance shifted by virtual origin and *(b)* mean temperature plotted with wall-normal distance shifted by virtual origin for temperature for case $S700$ denoted by solid lines and case $M700$ denoted by dashed line with circular markers. Red shows $Pr = 2$, blue shows $Pr = 1$ and green shows $Pr = 0.5$ cases.

The first step is to identify an appropriate length scale which governs the flow, $\ell$. Such a scale should satisfy two key requirements: it must be physically meaningful for the problem at hand, and it should yield velocity and temperature shifts that are single-valued, monotonic functions.

In the context of turbulent flow over perforated plates, Shahzad *et al.* (2022, 2023) demonstrated that the wall-normal Forchheimer permeability provides the best agreement with Nikuradse's data for higher values of $1/\alpha_y^+$.

In the present study, however, the choice of a representative length scale is more challenging, as the porous lattices exhibit non-zero permeability in all three spatial directions.Therefore, $\ell^+$ could be a combination of the Darcy and Forchheimer permeabilities in the i-th spatial direction,

$$\ell^+ = A_i\sqrt{K_i^+} + B_i/\alpha_i^+. \tag{2}$$

To find the coefficients in 2, we fit the present $\Delta U^+$ data to Nikuradse's sand grain roughness data, thus we effectively set $\ell^+ = k_s^+$, where $k_s$ is the sand grain roughness height. In this process we use an analytical two-parameter fitting function,

$$\Delta U^+(k_s^+) = \frac{1}{p\,\kappa}\ln\left(1 + x(k_s^+)\right) + \left(\frac{1}{\kappa}\ln C + A - B\right)\frac{x(k_s^+)}{1 + x(k_s^+)}, \tag{3}$$

where $x(k_s^+) = (k_s^+/C)^p$, $p = 2.28$ and $C = 12.37$ are the fitting constants, $A = 4.17$ is the smooth wall intercept, $B = 7.9$ is Nikuradse's constant, and $\kappa = 0.387$. This model is a modification of the one-parameter model proposed by Cheng *et al.* (2020),

$$\Delta U^+ = \frac{1}{p\kappa}\ln(1 + \beta(k_s^+)^p), \tag{4}$$

where $\beta = \exp(p\kappa(A - B))$, $p = 4$ is a fitting constant, $B = 8$, $A = 4.5$. Both models approach the fully rough asymptote for large values of $k_s^+$ and the model by Cheng *et al.* (2020) coincides with Colebrook's law (Colebrook, 1939) for $p = 1$. Figure 7 shows that equation (3) accurately model Nikuradse's

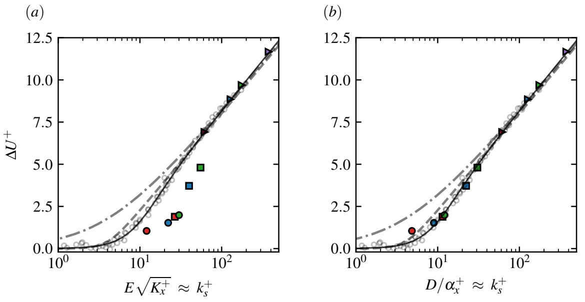


Figure 7. *(a)* The Hama roughness function $\Delta U^+$ variation with $11.6\sqrt{K_x^+} \approx k_s^+$, and *(b)* with $D/\alpha_x^+ \approx k_s^+$ where $D = 4.35$. The dash-dotted line shows Colebrook's law (Colebrook, 1939), the dashed black line shows the generalized roughness model (Cheng *et al.*, 2020), the solid black line shows the model fit for Nikuradse's data and the black markers show Nikuradse's sandgrain roughness data (Nikuradse, 1933)). Red circles show case $L260$, red squares are $M260$, red triangles are $H260$, blue circles are $L500$, blue squares are $M500$, blue triangles are $H500$, green circles are $L700$, green squares are $M700$, green triangles are $H700$ and purple triangles are $H1500$.

data across all values of $k_s^+$ and is slightly more accurate than equation (4) in the transitionally rough regime.

In this process, $1/\alpha_x^+$ emerges as the dominant term, followed by $\sqrt{K_x^+}$. Fitting using only the streamwise Forchheimer permeability we find $k_s^+ \approx 4.35/\alpha_x^+$, whereas using only the Darcy permeability $k_s^+ \approx 11.6\sqrt{K_x^+}$, see figure 7*(a)*. The Forchheimer permeability yields a closer fit to the sand grain roughness from the transitional to the fully rough regime, permitting a simple modelling framework for all regimes.

## Mean temperature deficit

Figure 8(*a*) shows the temperature deficit $\Delta\Theta^+$ plotted with $k_s^+ = 4.35/\alpha_x^+$. The DNS data by MacDonald *et al.* (2019) for flow over 3D sinusoidal roughness at $Pr = 1$ are reported, together with the results from the DNS by Peeters & Sandham (2019) for flow over irregular roughness at $Pr = 0.7$. The present data follow the same trend as the roughness data and it seems to approach a plateau for increasing $1/\alpha_x^+$, which is more evident at $Pr = 2$, at which we observe a slight decrease of $\Delta\Theta^+$ at the highest Reynolds number.

The modelling the temperature deficit in the fully rough regime has can be performed in terms of interfacial temperature $\Theta_i$ as in Brutsaert (1975), which is related to the temperature deficit as,

$$\Theta_i = \frac{1}{\kappa_\theta}\log y_i^+ + A_\Theta(Pr) - \Delta\Theta^+. \quad (5)$$

It should be noted here that $\Theta_i$ is the temperature at the start of the logarithmic layer. The main models for the interfacial temperature in the fully rough regime rely on a scaling in the form $\Theta_i \sim (k^+)^p Pr^m$, where $m = 0.5$ and $p = 1/2$ in the model by Owen & Thomson (1963) and $p = 1/4$ in the model by Brutsaert (1975). We compared this model to our DNS data in figure 7, where the interfacial temperature data is extracted at the point where the log-law intersects the DNS temperature profile. The figure confirms the exponents given by Brutsaert (1975), both for Prandtl number and for the roughness height, in particular, figure 7(*d*) shows an excellent match between DNS data and the following fit in the fully rough regime,

$$\Theta_i^+ = 1.2{k_s^+}^{1/4}Pr^{1/2} + 2.1. \quad (6)$$

Using equation (6) in (5), we find a model for the temeperature deficit, where we use $y_i \approx 0.58k_s^+$, which we measured from the DNS data.

As noted by Zhong *et al.* (2023), the scaling law (6) indicates that at sufficiently high values of $k_s^+$, $\Delta\Theta^+$ will start decreasing and even attain negative values, i.e., decreased heat transfer compared to smooth channel simulations.

Regarding the transitionally rough regime, we do not find a physics-backed model to represent it, but rather, we attempt an empirical model for the temperature shift,

$$\Delta\Theta^+ = C_1(Pr)\log(k_s^+) + C_2(Pr), \quad 0 < k_s^+ < k_{s,fr}^+ \quad (7)$$

where $C_1 = 2.46Pr + 0.53$ and $C_2 = -3.79Pr - 1.53$ are fitting constants depending on $Pr$. $k_{s,fr}^+$ is the onset of the fully rough regime, for which we use $k_{s,fr}^+ \approx 100$ and 70 at $Pr = 1$ and $Pr = 2$, respectively. For $Pr = 0.5$, there is no evidence of a fully rough regime.

## Conclusion

In this study, we carried out DNS of turbulent channel flow over cubic porous lattices using an immersed boundary method with periodic boundary conditions in the streamwise and spanwise directions and fully resolved porous geometries. We characterized the porous substrate using Stokes flow simulations to calculate the permeabilities. The virtual origin framework was used to align velocity and temperature statistics with smooth-wall references, with adjustments made for Prandtl number effects for the scalar quantities. The results revealed that with increasing porosity and $Re_\tau$, mean velocity profiles exhibited a downward shift in $\Delta U^+$, corresponding to enhanced drag. Mean temperature profiles showed similar downward shift, signifying an increase in heat transfer. The key findings of this work are the development of scaling laws that successfully predict these shifts. For velocity, we model Nikuradse's sandgrain roughness data using an analytical fitting function and we find out that $\Delta U^+$ from our simulations collapses with this model when scaled with the inverse of the streamwise Forchheimer permeability. Similarly, we modelled $\Delta\Theta^+$ using a logarithmic law in the transitional regime and a fully rough scaling at higher values of $1/\alpha_x^+$, by scaling $\Theta_i^+$ as a function of $1/\alpha_x^+$ and $Pr$. This work has also been extended to full-scale predictions of friction coefficient $C_f$ and Stanton number $St$, which has been omitted in the present paper due to space restrictions and will be elaborated upon in the presentation.

## REFERENCES

Breugem, W. P. & Boersma, B. J. 2005 Direct numerical simulations of turbulent flow over a permeable wall using a direct and a continuum approach. *Phys. Fluids.* **17** (2), 025103.

Breugem, W. P., Boersma, B. J. & Uittenbogaard, R. E. 2006 The influence of wall permeability on turbulent channel flow. *J.Fluid Mech* **562**, 35–72.

Brutsaert, W. 1975 The roughness length for water vapor sensible heat, and other scalars. *J. Atmos. Sci.* **32** (10), 2028–2031.

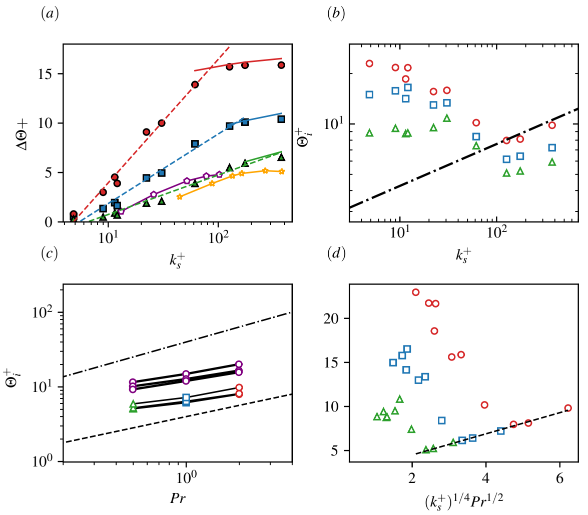


Figure 8. *(a)* Temperature deficit ($\Delta\Theta^+$) plotted with $k_s^+$, the dashed line shows the analytical fitting for the transitional regime, and the solid line shows the model for the fully-rough regime. The purple markers show the data for irregular roughness at $Pr = 1$ (Peeters & Sandham, 2019) and the orange markers show the data for sinusoidal roughness at $Pr = 0.7$ (MacDonald *et al.*, 2019); *(b)* Interfacial temperature ($\Theta_i^+$) plotted with $k_s^+$. The dash-dotted line shows the $(k_s^+)^{1/4}$ scaling law, which was seen in Zhong *et al.* (2023); *(c)* Interfacial temperature ($\Theta_i^+$) plotted with $Pr$, dashed line shows the 0.5 scaling, and dash-dotted line shows 0.67 scaling. The purple markers shows the $\Theta_i^+$ data for high $k_s^+$ values from Zhong *et al.* (2023); *(d)* $\Theta_i^+$ plotted with $(k_s^+)^{1/4}Pr^{1/2}$, dashed line shows the fully rough asymptote given by $\Theta_i^+ = 1.2(k_s^+)^{1/4}Pr^{1/2} + 2.1$. The red markers show $Pr = 2$ data, the blue markers show $Pr = 1$ and the green markers show $Pr = 0.5$ for the present cases. We do not distinguish between individual cases at a given $Pr$ for clarity; all such cases are represented using the same colour and marker.

Chandesris, M., D'Hueppe, A., Mathieu, B., Jamet, D. & Goyeau, B. 2013 Direct numerical simulation of turbulent heat transfer in a fluid-porous domain. *Phys. Fluids.* **25** (12), 125110.

Cheng, W., Pullin, D. I. & Samtaney, R. 2020 Large-eddy simulation and modelling of taylor–couette flow. *J.Fluid Mech* **890**, A17.

Chung, D, Hutchins, N, Schultz, M P. & Flack, K A. 2021 Predicting the drag of rough surfaces. *Annu. Rev. Fluid Mech.* **53** (Volume 53, 2021), 439–471.

Colebrook, C F 1939 Turbulent flow in pipes, with particular reference to the transition region between the smooth and rough pipe laws. *J. Inst. Civ. Eng.* **11** (4), 133–156.

Efstathiou, Christoph & Luhar, Mitul 2020 Turbulent boundary layers over streamwise-preferential porous materials.

Endrikat, S., Modesti, D., García-Mayoral, R., Hutchins, N. & Chung, D. 2021 Influence of riblet shapes on the occurrence of Kelvin–Helmholtz rollers. *J.Fluid Mech* **913**, A37.

Garcia-Mayoral, R. & Jimenez, J. 2011 Hydrodynamic stability and breakdown of the viscous regime over riblets. *J.Fluid Mech* **678**, 317–347.

Ibrahim, J. I., Gómez-de Segura, G., Chung, D. & García-Mayoral, R. 2021 The smooth-wall-like behaviour of turbulence over drag-altering surfaces: a unifying virtual-origin framework. *J.Fluid Mech* **915**, A56.

Kays, W. M. & Crawford, M. E. 1980 *Convective Heat and Mass Transfer*, 2nd edn. *McGraw-Hill Series in Mechanical Engineering* 1. New York: McGraw-Hill.

Khorasani, S. M. H., Luhar, M. & Bagheri, S. 2024 Turbulent flows over porous lattices: alteration of near-wall turbulence and pore-flow amplitude modulation. *J.Fluid Mech* **984**, A63.

Kuwata, Y. & Suga, K. 2019 Extensive investigation of the influence of wall permeability on turbulence. *Int. J. Heat Fluid Flow* **80**, 108465.

Kuwata, Y. & Suga, K. 2024 Reynolds number dependence of turbulent flows over a highly permeable wall. *J.Fluid Mech* **981**, A3.

Ligrani, P. 2013 Heat transfer augmentation technologies for internal cooling of turbine components of gas turbine engines. *Int. J. Rotat. Mach.* **2013** (1), 275653.

MacDonald, M., Hutchins, N. & Chung, D. 2019 Roughness effects in turbulent forced convection. *J.Fluid Mech* **861**, 138–162.

Manes, C., Poggi, D. & Ridolfi, L. 2011 Turbulent boundary layers over permeable walls: scaling and near-wall structure. *J.Fluid Mech* **687**, 141–170.

Nagib, H.M. & Chauhan, K.A. 2008 Variations of von Kármán coefficient in canonical flows. *Phys Fluids* **20** (10).

Nikuradse, J. 1933 Strömungsgesetze in rauhen rohren. *VDI-Forschungsheft* **361**.

Nishiyama, Y., Kuwata, Y. & Suga, K. 2020 Direct numerical simulation of turbulent heat transfer over fully resolved anisotropic porous structures. *Int.J.Heat Fluid Fl.* **81**, 108515.

Owen, P. R. & Thomson, W. R. 1963 Heat transfer across rough surfaces. *J.Fluid Mech* **15** (3), 321–334.

Peeters, J.W.R. & Sandham, N.D. 2019 Turbulent heat transfer in channels with irregular roughness. *International Journal of Heat and Mass Transfer* **138**, 454–467.

Pirozzoli, S. & Modesti, D. 2024 Mean temperature profiles in turbulent internal flows. *Int. J. Heat Fluid Flow* **109**, 109544.

Shahzad, H., Hickel, S. & Modesti, D. 2022 Permeability and turbulence over perforated plates. *Flow, Turbulence and Combustion* **109** (4), 1241–1254.

Shahzad, H., Hickel, S. & Modesti, D. 2023 Turbulence and added drag over acoustic liners. *J.Fluid Mech* **965**, A10.

Suga, K., Mori, M. & Kaneda, M. 2011 Vortex structure of turbulence over permeable walls. *Int. J. Heat Fluid Flow* **32** (3), 586–595.

Suga, K., Nakagawa, Y. & Kaneda, M. 2017 Spanwise turbulence structure over permeable walls. *J.Fluid Mech* **822**, 186–201.

Yaglom, A. M. & Kader, B. A. 1974 Heat and mass transfer between a rough wall and turbulent fluid flow at high reynolds and péclet numbers. *J.Fluid Mech* **62** (3), 601–623.

Zhong, K., Hutchins, N. & Chung, D. 2023 Heat-transfer scaling at moderate prandtl numbers in the fully rough regime. *J.Fluid Mech* **959**, A8.